



OPEN

Selective electrochemical reduction of CO₂ on compositionally variant bimetallic Cu–Zn electrocatalysts derived from scrap brass alloys

Ibrahim M. Badawy¹, Ahmed Mohsen Ismail¹, Ghada E. Khedr^{1,2}, Manar M. Taha¹ & Nageh K. Allam¹✉

The electrocatalytic reduction of carbon dioxide (CO₂RR) into value-added fuels is a promising initiative to overcome the adverse effects of CO₂ on climate change. Most electrocatalysts studied, however, overlook the harmful mining practices used to extract these catalysts in pursuit of achieving high-performance. Repurposing scrap metals to use as alternative electrocatalysts would thus hold high privilege even at the compromise of high performance. In this work, we demonstrated the repurposing of scrap brass alloys with different Zn content for the conversion of CO₂ into carbon monoxide and formate. The scrap alloys were activated towards CO₂RR via simple annealing in air and made more selective towards CO production through galvanic replacement with Ag. Upon galvanic replacement with Ag, the scrap brass-based electrocatalysts showed enhanced current density for CO production with better selectivity towards the formation of CO. The density functional theory (DFT) calculations were used to elucidate the potential mechanism and selectivity of the scrap brass catalysts towards CO₂RR. The d-band center in the different brass samples with different Zn content was elucidated.

To mitigate the harmful effects of climate change, the scientific community is pursuing a vision for sustainability that falls under the planetary boundaries. High energy demand has led to the overconsumption of fossil fuels and excess carbon dioxide (CO₂) emissions^{1,2}. The excessive mining of minerals, as well, due to general poor regulation is entangled in a web of environmental and societal harm^{3,4}. Hence, considerable research work is directed towards steering away from the mining of metals and combustion of fossil fuels into greener alternatives^{5,6}. Developing a solution that will make use of renewable energy sources and building a basis for affordable recycling schemes are the key to a sustainable future^{7,8}.

Thus, as a promising step towards closing the carbon cycle, the electrocatalytic CO₂ reduction reaction (CO₂RR) has garnered vast research interest. Despite proving to be a complex reaction, many studies have demonstrated strong results using a wide variety of electrocatalysts^{9–14}. The underlining goal for these studies is to eventually scale this process whereby it can compete with the existing energy production methods. Making decisions aimed towards minimizing both capital and running costs are therefore essential considerations. With regards to the latter, converting CO₂ directly to higher hydrocarbons (C₂₊) using copper (Cu), the catalyst of choice, is a challenging task. Namely because Cu is not selective and produces a variety of hydrocarbons with poor faradic efficiencies (FE)¹⁵. From an industrial standpoint, it is preferable to produce a single product at high FE rather than many at low FE because it would spare separation costs. Another challenge is by converting CO₂ directly into CH₄ one faces high overpotentials, which can be a significant source of inefficiency¹⁶. Techno-economic models suggest an indirect pathway for the production of hydrocarbons via carbon monoxide (CO) can be more practical in light of commercial viability^{17–19}. Moreover, well-established industrial processes, such as Fischer–Tropsch, utilize direct CO-based feedstock²⁰. Thus, CO as a product of CO₂RR in many respects is more favorable over hydrocarbons.

On the other side of the equation, cheap and abundant catalyst materials must also be considered to minimize capital costs. The best, consistently performing catalysts for CO production are Pd, Au, and Ag^{11,21,22}. However, designing a catalyst from noble metals alone is not cost-effective. Brass, on the other hand, is vastly available,

¹Energy Materials Laboratory (EML), School of Sciences and Engineering, The American University in Cairo, New Cairo 11835, Egypt. ²Department of Analysis and Evaluation, Egyptian Petroleum Research Institute, Cairo 11727, Egypt. ✉email: nageh.allam@aucegypt.edu

cheap, and possesses no environmental concerns. Many studies have demonstrated promising results with brass as an electrocatalyst for CO₂RR^{12,23–31}. A metal–organic framework (MOF) derived electrocatalyst with Cu and Zn bimetallic centers generated CO with 88% FE. The phthalocyanine molecule facilitated the synergism between CuN₄ and ZnO₄ centers to produce CO at a high rate³². In another study, oxidized brass nanoparticles supported on carbon nanotubes (CNT) were synthesized using a multistep calcination method. They reported ≈ 50% FE for CO and ≈ 90% FE for syngas³³. Despite the promising performance of brass-based nanoparticles, their scaling can be challenging and costly due to the requirement of specialized chemicals and precise synthesis techniques. Therefore, nanoparticles are not always the most practical from an industrial standpoint^{34,35}. Consequently, nanofoams and structures were produced directly from metal foils^{5,26,27}. Stojkovic et al. prepared bronze nanofoam via high potential processing. The structure consisted of dendrites that substantially increased the surface roughness, resulting in an improvement in CO FE from 35–40% to ≈ 85%³⁶. However, the production of nanofoam requires extremely high current densities, which is a cost burden, especially at the industrial scale^{37,38}. To this end, the direct use of metal scraps without the need for expensive processing seems to be the most cost-effective and environmentally sustainable alternative. Moreover, despite the high reported activity of different Cu–Zn-based electrocatalysts in CO₂RR, the effect of alloying them with another metal on the CO₂ reduction performance is still lacking³⁹.

Herein, we explore the use of scrap brass alloys with different Zn content CO₂RR as a basis for the development of a new platform of recycled electrocatalysts. The activity and selectivity of brass catalysts were enhanced using inexpensive methods and through the controlled deposition of Ag, which stabilizes ZnO and introduces more active sites for CO production. In addition, density functional theory (DFT) simulations have been employed to help understand the mechanism by which the catalysts facilitate the formation of CO and its selectivity over other products.

Material and methods

Materials. Ammonia 25%, ammonium sulfate (≥ 99.0%), and silver nitrate (≥ 99.0%) were obtained from Sigma Aldrich. Potassium bicarbonate (99%) was obtained from Alfa Aesar. The brass alloys of different compositions were cut into 1.5 × 3.0 cm sheets. All reagents were used without further purification. MilliQ ultrapure water was applied throughout the study.

Pre-treatment of brass alloys. The samples (1-CuZn with 5% Zn, 2-CuZn with 15% Zn, 3-CuZn with 30% Zn, and 4-CuZn with 50% Zn) were polished with 1200 grit sandpaper until a smooth, mostly homogenous surface was obtained. Next, they were sonicated for 2 min, once in ethanol and then in distilled water. Finally, the samples were annealed in the air for one hour at 500 °C with a rate of 10 °C/min. The bulk composition of the samples was analyzed by energy dispersive x-ray (EDX) measurements, see Fig. S5.

Galvanic replacement. Ag was deposited via galvanic replacement. A solution of 50 mL of 1.68 M NH₄OH was prepared, then 7.664 g of (NH₄)₂SO₄ and 0.8494 g of AgNO₃ were added, and the mixture was continuously stirred. The metal scrap was dipped inside the prepared solution for a timed number of seconds.

Electrochemical measurements and product analysis. The electrochemical CO₂ reduction reaction was carried out in a glass gas-tight H-type cell with two compartments separated by a proton exchange membrane (Nafion 117). A Biologic SP300 type potentiostat/galvanostat was used for all electrochemical experiments in a 3-electrode set-up. The counter electrode used was a platinum coil, and the reference electrode was Ag/AgCl (KCl sat.). Unless otherwise stated, the electrolyte used for all measurements was aqueous 0.5 M KHCO₃ for both the cathode and anode compartments, which was bubbled with 99.999% CO₂ for 30 min. The catholyte was continuously stirred and had a volume of 40 mL. The measured potentials were converted to the reversible hydrogen electrode (RHE) reference scale using the formula. $E_{\text{RHE}} = E_{\text{Ag/AgCl}} + 0.197 \text{ V} + 0.059 \text{ pH}$. All currents were normalized to the geometric surface area of the electrodes. The pH of the electrolyte was measured to be 7.5. During the chronoamperometry measurements, the gas phase products were quantified by a gas chromatography (SRI 8610C Multi-gas #5, 6' Haysep D and 6' Molecular Sieve 5A) that was directly connected to the cathodic compartment via the online sampling loop. The gas chromatography was equipped with a thermal couple detector (TCD), and a flame ionization detector (FID) with Argon (99.9999%) applied as the carrier gas. The liquid phase products were quantified using High-Performance Liquid Chromatography (HPLC, Eclipse XBD-C18) with a flow rate of 0.6 mL/min and HPLC grade acidified deionized water as the mobile phase.

Materials characterization. The morphology of the brass samples was characterized by Zeiss SEM Ultra 60 field emission scanning electron microscope (FESEM) with 8 kV applied voltage, and the elemental composition was determined using energy dispersive X-ray analysis (EDX) attached to the SEM equipment. Rigaku SmartLab X-ray diffractometer was used to record the grazing incident x-ray diffraction (GIXRD) spectra in the 2θ range of 5°–80° at step rate of 0.007°.

DFT calculations. For the DFT calculations, the standard Cambridge Serial Total Energy Package (CASTEP) implemented in Materials Studio version 2017 was used⁴⁰. We began with Cu₃Zn unit cell, then a (3 × 3) supercell was created to simulate the four different structures. A (111) surface was cleaved, which was chosen based on the experimental results. A vacuum slab of 15 Å was included to avoid interaction with its image. For the Ag-coated 3-CuZn, a cluster of four Ag atoms was added on the top layer. The top and bottom layers and the adsorbate were allowed to relax, while the middle two layers were fixed. All spin polarized calculations were performed

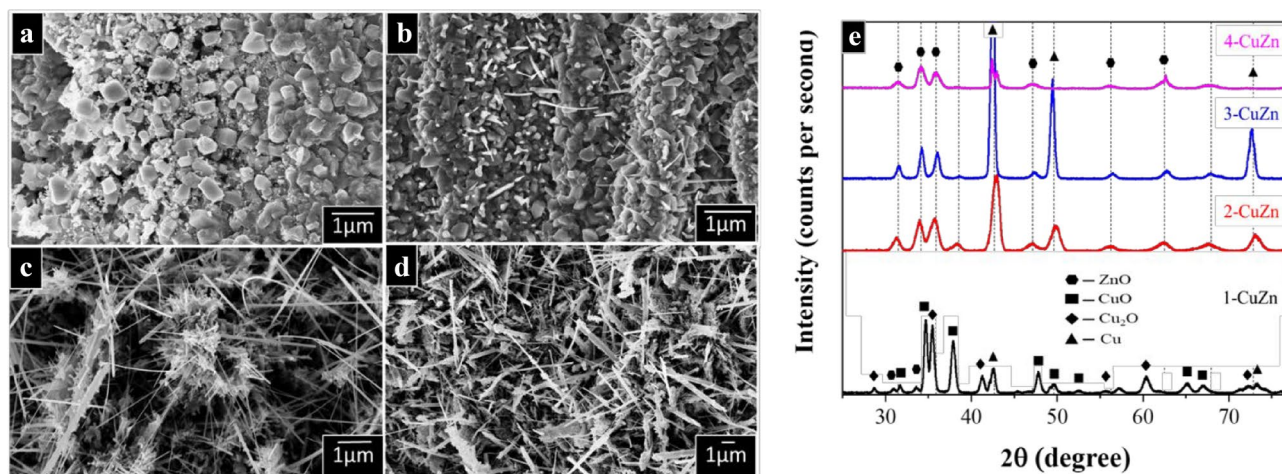


Figure 1. SEM images of the (a) 1-CuZn with 5% Zn, (b) 2-CuZn with 15% Zn, (c) 3-CuZn with 30% Zn, and (d) 4-CuZn with 50% Zn samples after annealing in air at 500 °C for 1 h. (e) Grazing angle XRD patterns for all 4 samples after annealing at 500 °C for 1 h with 10 °C/min heating rate.

using the generalized gradient approximation of Perdew, Burke and Ernzerhof (GGA-PBE) with ultrasoft pseudopotential. The cutoff energy was set to 400 eV with a convergence criterion of 5×10^{-6} eV/Å, maximum force 0.01 eV/Å, maximum stress 0.02 GPa, maximum displacement 5×10^{-4} Å and the Monkhorst-pack k-points sampling was set to a $2 \times 2 \times 1$ grid. We also did transition state (TS) search using complete Linear Synchronous Transit/Quadratic Synchronous Transit (LST/QST) protocol with root mean squared (RMS) convergence of 0.01 eV/Å to identify the energy barriers for the reaction. The nudged elastic band (NEB) calculations were done to confirm the transition states of the reaction.

Regarding the effect of the solvent and solvation of CO_2 , the following correction factors were used; -0.51 eV, 0.13 eV, 0.25 eV and 0.5 eV for the species CO^* , CO_2^* , COOH^* and OH^* , respectively. This is a common practice for CO_2 RR computational modeling as it spares computational cost considerably^{41,42}. To further confirm the accuracy of this correction of the PBE-gas phase, we performed pilot calculation for CO^* using COSMO solvent model for aqueous solvent with a dielectric constant of 78.54, where the difference was found to be within 0.1.

Results and discussion

Characterization analysis. The scrap brass specimens were annealed at 500 °C in the air to oxidize the surface and allow for nanostructuring^{43–46}. Upon increasing the Zn content in the brass sample, the annealing resulted in the formation of different nanostructures, see Fig. 1. The sample with the least Zn content (5% Zn) shows the formation of distorted nanocubes on the surface (Fig. 1a), which are typically observed for CuO and Cu_2O ⁴⁷. Upon increasing the Zn content, nanoneedles start to form on the surface of all samples, which may be attributed to the formation of ZnO with hexagonal lattice structure^{48,49}. Note that Zn has a higher oxidation affinity than Cu⁵⁰. Therefore, upon heating, Zn atoms diffuse to the surface along the grain boundaries, where they are then oxidized and form the nanoneedle structures. The density of nanoneedles on the surface increases with increasing the Zn content (Fig. 1b–d).

To better understand the crystal structure and composition of the formed phases, glancing angle XRD patterns were recorded. Figure 1e indicates the formation of Cu_2O and CuO for sample 1-CuZn and to a lesser degree for sample 2-CuZn. The diffraction peaks of Cu_2O (JCDPS: 96-100-0064) were observed at 29.6° (110), 36.5° (111), 42.3° (200), 62.4° (220), and 73.6° (311). The most pertinent peaks of CuO (JCDPS: 96-110-0029) appeared at 32.66° (110), 35.4° (002), 38.86° (111), 48.9° (−202), 66.6° (−311), and 68.4° (220). These peaks were absent for samples 3-CuZn and 4-CuZn. The peaks observed at 31.8° (100), 34.4° (002), 36.2° (101), 56.5° (110), and 62.8° (103) can be assigned to the hexagonal phase of ZnO crystals (JCDPS: 96-153-7876). Although no peaks of metallic Zn were observed, the peak at 44.7° is characteristic of metallic Cu (111), which can be related to the fact that Zn has a higher oxidation potential and is thus more readily oxidized than Cu. As the Zn content in the base alloy increases, it oxidizes quickly, dominating the surface and leaving Cu metal underneath. The estimated grain size from the peak broadening of the ZnO (Table S1) indicates that there is no pronounced difference between the samples. Furthermore, the lattice microstrain, estimated from the peak broadening, is very low, suggesting the little formation of defects in the crystal structure^{51,52}.

Electrochemical CO_2 RR. The annealed scrap brass samples were implemented directly into the electrochemical system to study their efficiency as catalysts for CO_2 RR. The performance of the brass scraps was first studied using linear sweep voltammetry (LSV), as shown in Fig. 2. The experiments were conducted in CO_2 -saturated 0.5 M KHCO_3 and in Ar-saturated 0.5 M Na_2SO_4 electrolytes under continuous bubbling of the respective gas. The samples were pre-scanned at 10 mV/s for 5 cycles to ensure they reached equilibrium and stabilized before recording their actual response. Figure S1 reveals a broad peak for all the four samples under Ar bubbling in the potential range of -0.6 to -0.4 V vs. RHE, which can be attributed to the reduction of Cu_2O ⁵³.

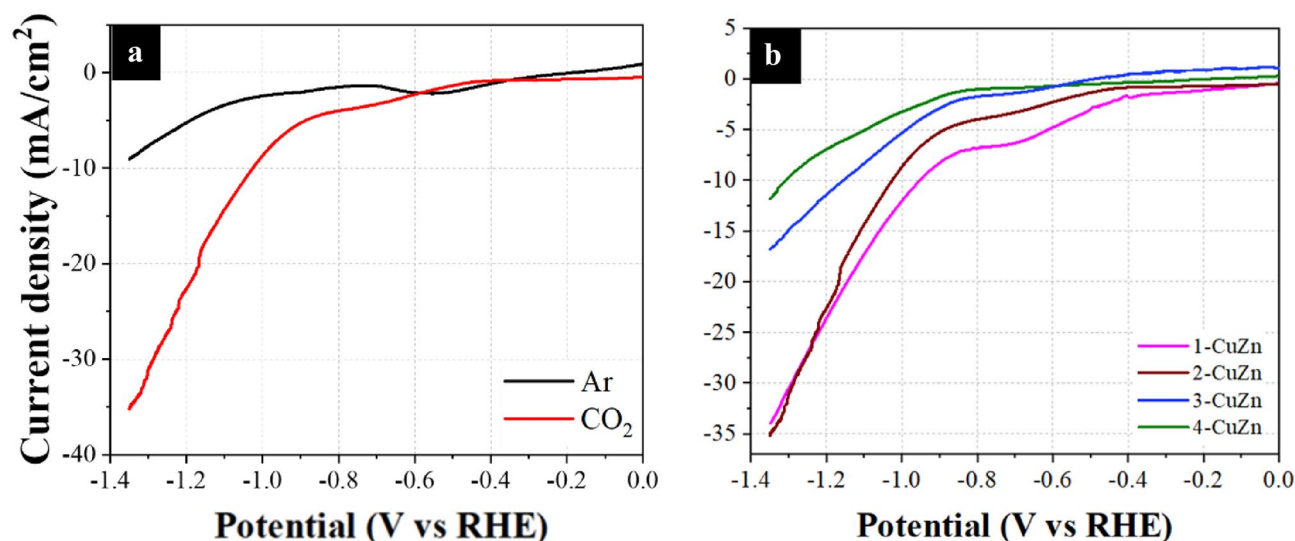


Figure 2. Linear scan voltammetry under continuous CO_2 and Ar purge in 0.5 M KHCO_3 and 0.5 M Na_2SO_4 , respectively for samples (a) 1-CuZn, (b) 2-CuZn, (c) 3-CuZn, and (d) 4-CuZn.

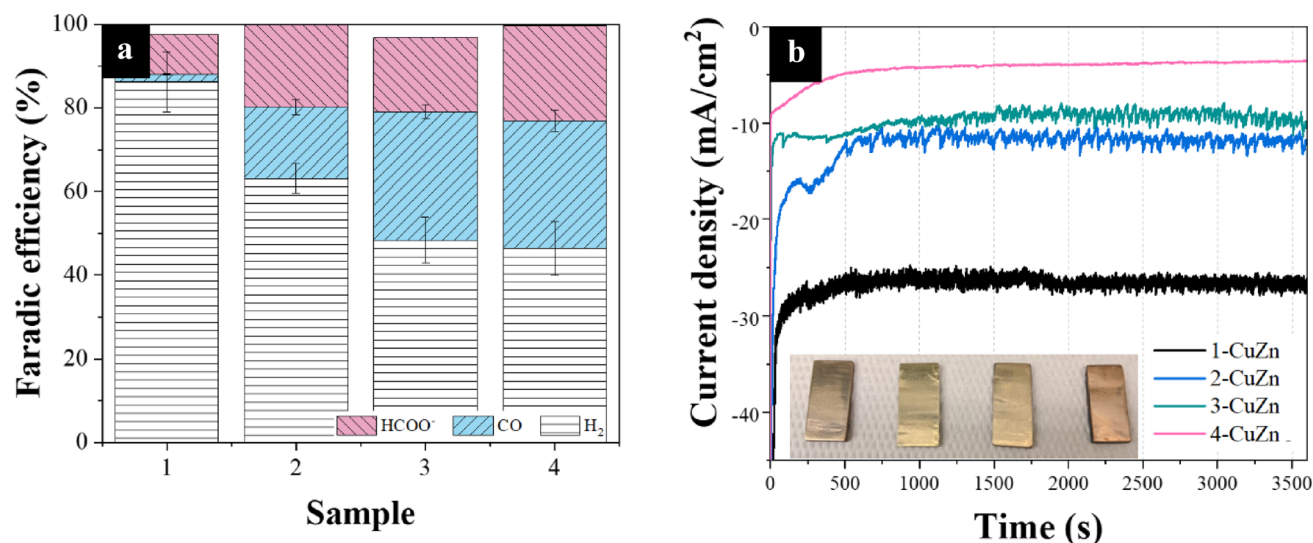


Figure 3. The electrocatalytic performance of the samples at a potential of -0.91 V vs. RHE. (a) The measured Faradic efficiencies and (b) the chronoamperometry profiles with an inset of a photograph of the 4 polished brass samples.

The curve of sample 4-CuZn, however, shows a different peak between -1 and -0.8 V vs. RHE, which is likely ascribed to the reduction of ZnO ⁵³. Table S2 shows the extracted data from the LSV curves for each sample. It is also worth noting that at 0 V vs. RHE, the electrocatalysts showed non-zero current, likely because of double-layer charging and parasitic reactions at the surface of the electrode. It is difficult to eliminate these effects as LSV cannot distinguish between electrocatalyst, electrolyte, and charge transfer events⁵⁴.

The onset potential for the samples tested under CO_2 shifts towards more negative potentials as the Zn content increases (from -0.17 to -0.851 V vs. RHE). This is likely due to the ability of Zn to suppress the hydrogen evolution reaction (HER), which is observed in Fig. 3a as well, where the FE of H_2 is much less for the samples with high Zn content as compared to the samples with lower Zn content^{55,56}. Not to mention that the difference in the current density generated between the curves under CO_2 bubbling and Ar bubbling progressively becomes more pronounced as the Zn content increases. This is strong indication that most of the current density generated by sample 1-CuZn in the LSV is due to HER where the difference between the CO_2 condition and Ar is least. Nevertheless, the onset potential is only a guiding parameter that should not be over-interpreted because it can be influenced by parasitic reactions and system sensitivity⁵⁷. All in all, the addition of Zn to Cu, despite increasing the onset potential, minimizes the production of HER.

The surface roughness (Table S3) coincides quite well with the obtained current density for each sample. Sample 1-CuZn has the highest roughness of 134.5 and, as a result, demonstrates one of the highest total current

densities of 30 mA/cm² at -0.91 V vs. RHE. However, most of this current is consumed by the HER, which is a high competitor with CO₂RR (Supplementary information Fig. S3). It is worth mentioning that surface roughness often influences the performance of the catalyst beyond just the value of the current density, namely the product selectivity. Hence, the early development of current observed in the LSV is most likely attributed to HER overwhelming the surface rather than CO₂RR^{15,58,59}. In our case, changing the Zn content is not only influencing the chemical nature of the catalyst but also the physical nature, i.e., the electrochemical active surface area (EASA)^{60,61}. CO₂RR relies on complicated mass transport equilibria within the buffer electrolyte and, as such, faces many kinetic barriers^{62,63}.

Figure S3 shows the calculated FE of each of the samples over the measured potential range, which reveals a weak dependency between the FE and applied potential. Figure 3a shows the FEs at -0.91 V vs. RHE. Samples 3-CuZn and 4-CuZn show the highest CO FE, reaching 30.8% and 30.6%, respectively, which means both samples share similar product selectivity. The difference of product selectivity between samples 3-CuZn and 4-CuZn is insignificant and the progression of Zn content with respect product FE leads to a plateau rather than a volcano shape. This suggests a saturation of activity with the addition of Zn beyond 30%. As for the reaction rate, sample 3-CuZn has the larger total current density yielding an average of 10.16 mA/cm² at -0.91 V vs. RHE throughout the 3600 s compared to 3.66 mA/cm² for the 4-CuZn sample as shown in Fig. 3b. The decreased rate activity of 4-CuZn compared to 3-CuZn has been further investigated using density functional theory (DFT) simulations as discussed in a subsequent section.

It is well-established in the literature that Zn-based electrocatalysts tend to produce HCOO⁻ as a liquid product, which is also observed with our brass electrocatalysts upon HPLC analysis of the electrolyte^{26,64,65}. The results in Fig. 3a show that the sample with the least Zn content (1-CuZn) produced the least FE for HCOO⁻ at 9.68%, while the sample with the highest Zn content (4-CuZn) produced the highest FE at 22.6%. Note that CO production likely takes place on the ZnO sites, while HCOO⁻ production takes place on the reduced ZnO sites^{66,67}. As a -1.10 V vs. RHE potential (i.e., the reduction potential of Zn(II) at this particular pH) is applied, ZnO would always be reduced during the CO₂RR experiment. In our case, CO₂RR begins at -1.16 V vs. RHE, which makes the production of HCOO⁻ nearly unavoidable. This is further revealed from the XRD patterns in Fig. 4c of the samples after electrolysis, revealing the almost complete disappearance of the ZnO peaks, especially for samples 3-CuZn and 4-CuZn. This makes the selectivity control with respect to Zn very difficult and urges more designs to overcome such a challenge. The Cu₂O and CuO have also disappeared due to the applied reduction bias. The state of the Cu however is likely a partially reduced phase between Cu₂O and Cu metal as previously reported in the literature⁵⁴.

Modification by Ag. To improve the selectivity, Ag was deposited on the surface of the brass samples with the assumption that Ag would stabilize the oxide species where its reduction would be minimized as well as introduce more active sites for CO production. Upon Ag deposition, sample 3-CuZn showed the best FE for CO production. The successful deposition of Ag was confirmed by the new Ag diffraction peaks that appeared at 39.56° (111), 45.74° (200), and 66.11° (220), as depicted in Fig. 5c. A new diffraction peak emerged at 44.34°, which is characteristic of AgZn, revealing the strong affinity of Ag towards Zn that is expected to impact the chemical nature of the overall electrocatalyst during the CO₂RR⁶⁸. Indeed, the results depicted in Fig. 4b, show the decrease in the formation of HCOO⁻ from 21.6 to 7.53% after 5 s, and to 4.68% after 20 s until it becomes undetectable by the HPLC after 60 s. The XRD pattern (10) in Fig. 2c also shows the preservation of the ZnO peaks after CO₂RR. Furthermore, Fig. S4a,b shows the SEM images of sample 3-CuZn after Ag deposition as indicated by the emerged rhombic features. Note that those features are retained after the CO₂RR, revealing the role played by Ag in stabilizing ZnO, whereby it is able to withstand the reduction potentials of CO₂RR. Ag can also promote CO production by introducing more active sites, as revealed in Fig. 4a. As the Ag deposition time increases, the partial current density, which can be approximated to the rate of CO production, also increases until reaching a maximum of 3.44 mA/cm² in the time interval of 20–30 s. Thus, the addition of Ag improved the selectivity of 3-CuZn towards CO production. To complete the picture for the Ag deposited on brass, a stability measurement was performed as shown in Fig. 4d. The measurement was performed for 6 h, where the electrocatalyst maintained good stability throughout the test.

DFT modeling and analysis. As previously discussed, annealing the scrap brass samples in the air tends to form electrocatalysts that favor the formation of CO and CHOO⁻. In this regard, DFT calculations were performed to gain insights into the mechanism of the reaction as well as to explain the difference in activities between the samples⁶⁹. CuZn (111) surface was studied in particular because it consistently showed the strongest peaks in the XRD spectra of the annealed samples (Fig. 1c). The sequence of CO₂RR on the brass surface proceeds as depicted in Fig. 5a. Upon CO₂ adsorption, Mulliken's charge analysis reveals the charge transfer from 3-CuZn (111) surface to the CO₂ molecule. As a result, the CO₂ molecule gains a negative charge of 0.52 e and forms a negatively charged CO₂ anion. This leads to strong adsorption on the catalyst surface. As the reaction continues, the two C–O bond lengths are elongated, and the (O–C–O) angle is decreased from 180° to 135.9°, revealing the activation of CO₂. To unveil the mechanism of the dissociation of CO₂ on the 3-CuZn (111) surface, the following three possible routes for dissociation were elucidated: the direct dissociation and the H-assisted dissociation (the hydrogen source is the electrolyte in this case)^{70,71}. Figure 5a shows the direct dissociation route, where the interaction between the 3-CuZn (111) surface and CO₂ spontaneously forms CuZn-CO₂* that is then dissociated to CuZn-CO* + O* via the transition state (TS₁). This process is exothermic by -0.04 eV and has an activation barrier of 1.48 eV. After that, absorption of 0.8 eV from ambient heat leads to the desorption of CO* from the surface to form CO gas. The second possible dissociation route is the H binding. In the presence of hydrogen, CO₂ may be activated towards the formation of COOH* or HCOO*. In the case of carboxyl forma-

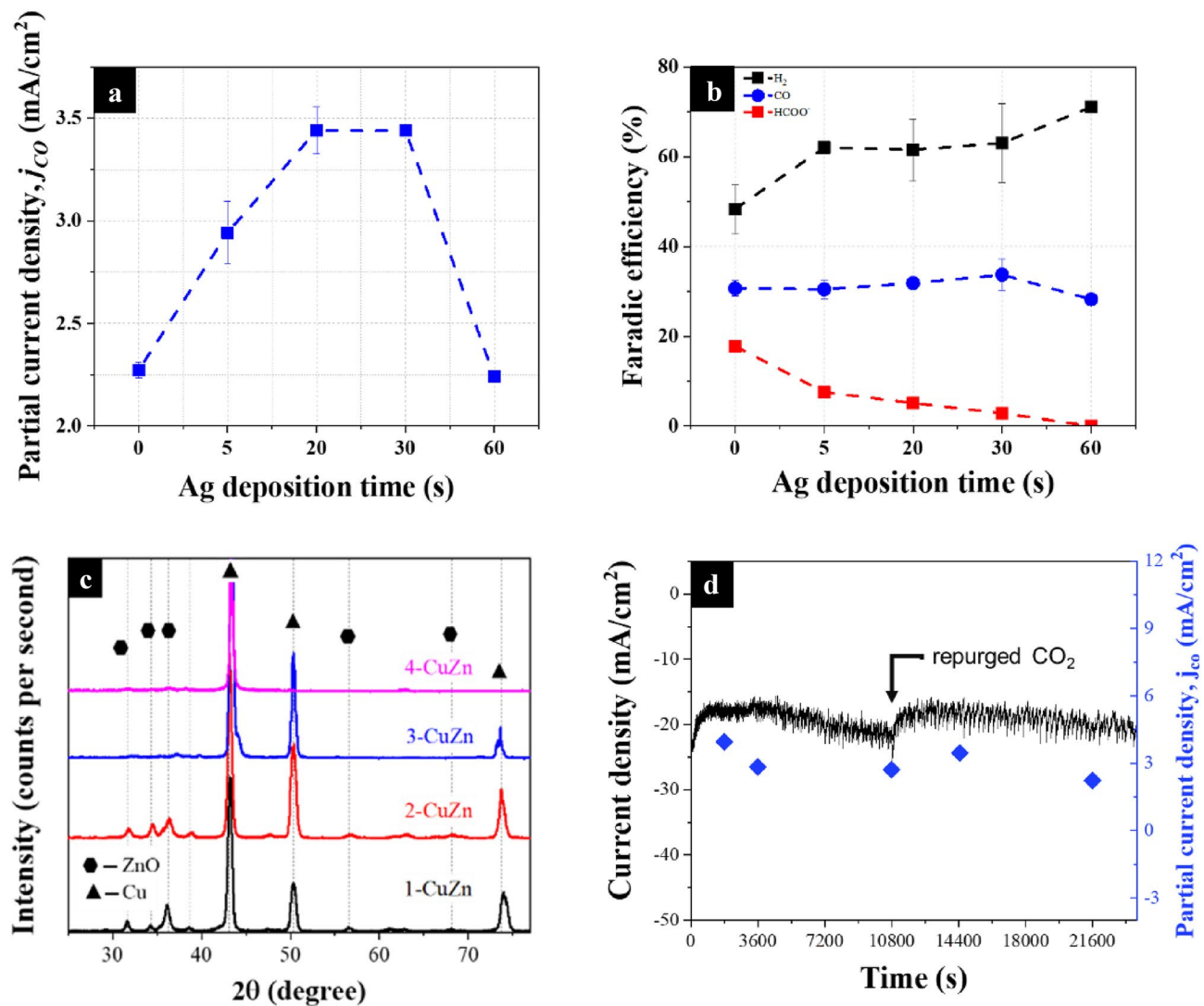


Figure 4. (a) The partial current densities of CO across different Ag deposition times at -0.91 V vs. RHE for sample 3-CuZn (b) Faradic efficiency and the ratio of product gases of 3-CuZn with different Ag depositions times at -0.91 V vs. RHE (c) Grazing angle XRD patterns for all samples after electrochemical CO₂RR at -0.91 V vs. RHE (d) stability showing the current density and partial current density for 3-CuZn with 20 s Ag deposition at -0.91 V vs. RHE.

tion, hydrogen atom attacks one of the oxygen atoms of the CO₂ and forms O–H bond, as depicted in Fig. 5a. This step passes through a transition state (TS₂) of 1.49 eV. This step is endothermic by 0.32 eV followed by breaking of the C–O bond and forming adsorbed CO* and OH* via (TS₃) of 0.55 eV. This process is exothermic by 0.47 eV. Concerning the formation of formate route, hydrogen atom binds to the carbon atom of CO₂ through a transition state (TS₄) of 1.03 eV, which is an exothermic process of 0.64 eV. Then it splits into HCO* and O* followed by hydrogen transfer to the O* to form CO* and OH* through a barrier of 0.55 eV. The adsorbed CO* desorbs in the gaseous form by 0.93 eV. Although both pathways are viable, our results reveal that the direct dissociation is more thermodynamically favorable. It is also important to note that this particular catalyst surface does not promote C–C coupling, which also would explain the lack of C₂₊ products in the experimental tests. The three mechanisms are shown in more detail in supplementary information Figs. S10–S14.

In order to better understand the selectivity and activity of the electrocatalysts, calculations of the electronic states for all the four different samples (1-CuZn, 2-CuZn, 3-CuZn, 4-CuZn) and Ag-coated 3-CuZn were carried out. Figure 5b shows the projected density of states (PDOS) for Cu atom in each system and its d-band center (ϵ_d). The position of the d-band center with respect to the Fermi level is important because it indicates the availability of electrons in the atom⁷². Thus, ϵ_d is strongly correlated to the binding energy, and it is often used as a metric for catalytic activity⁷³. A ϵ_d that is closer to the Fermi level pushes the antibonding states above the Fermi level where they will be less filled and hence stronger binding between the catalyst and the adsorbed intermediates^{74,75}. The four samples along with the Ag deposited sample show relatively close ϵ_d values as seen in Fig. 5b. The largest difference in the samples' d-band is 0.69 eV between 3-AgCuZn and 1-CuZn which suggests that the electronic effect on the performance of the electrocatalysts might not have profound overall impact^{42,76}.

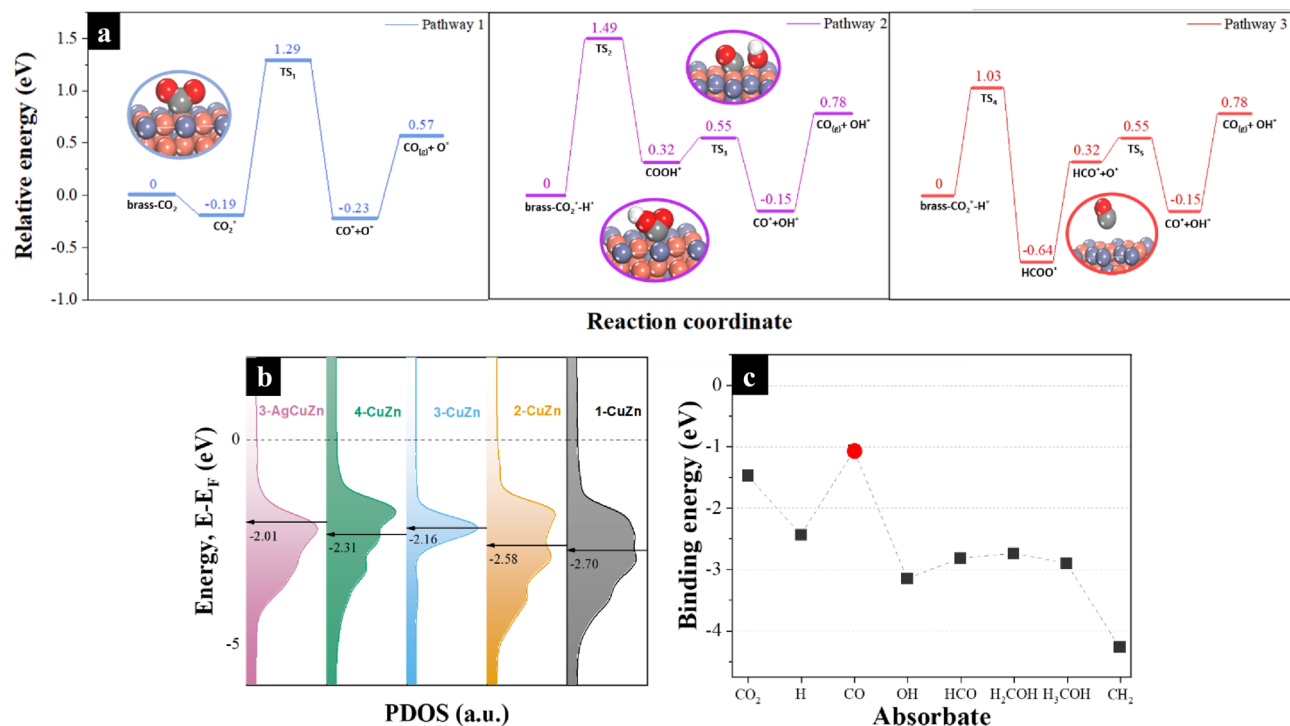


Figure 5. (a) Potential energy profile of the mechanism for the three proposed pathways for CO formation on sample 3-CuZn: direct dissociation, H-assisted via COOH*, and via HCOO*. (b) The projected density of states (PDOS) of the Cu atom in the four samples on the (111) plane and the d-band center represented by the black arrow while the Fermi level is the dotted line, and (c) the binding energy of the different adsorbates during CO₂RR on the Ag–CuZn (111) surface, the red dot is the binding energy of CO.

The more dominant parameter is perhaps the geometric differences between each of the catalysts' nanostructures as discussed in characterization analysis. This coincides with the experimental findings in a very specific way; the addition of Ag to the best performing sample, 3-CuZn, did not impact the FE towards CO significantly but rather impacted the partial current density for CO. This enhanced activity for CO specifically is likely owed to the structural changes induced by the Ag rather than the chemical.

As for the selectivity (i.e. the chemical nature) towards CO production specifically, Fig. 5c depicts the binding strength of the different adsorbates that are likely to form during the CO₂RR process on the most energetically favorable site on the 3-AgCuZn surface. The CO molecule, which is represented by the red dot, has the least binding energy among all the other possible products especially the products that are rank higher in electron transfers. This suggests that its desorption of CO after its formation is the more likely event rather than its further reaction. This is indeed what is observed experimentally as the formation of formate is decreased substantially while the formation of CO is enhanced.

Conclusion

A simple, inexpensive, and scalable method to repurpose scrap brass metal alloys for CO₂RR to produce syngas at a reasonable rate was demonstrated. Scraped brass samples with different Zn content were activated via annealing in an air atmosphere, where various nanostructures emerged. Increasing the Zn content led to the formation of denser nanoneedles. As revealed via the XRD analysis, the formation of ZnO was found to inhibit the HER and promote the formation of both CO and CHOO. The Faradic efficiency (FE) of the samples showed weak dependency on voltage. This should be beneficial from an industrial perspective as it is hard to control the working electrode potential in real electrolyzers, where no reference electrodes are being used. The 3-CuZn electrocatalyst with 30% Zn was found to be the best performing among all tested samples with FEs of 30.7% and 21.6% for CO and CHOO⁻, respectively. The addition of Ag improved the performance of the electrocatalyst by increasing the partial current density towards the formation of CO. The DFT calculations confirmed the obtained experimental results in terms of possible formed intermediates and calculated d-band center (ϵ_d). The brass alloy modified by Ag showed the lowest binding energy for CO indicating its facile release and preferred production over any other product.

Received: 10 June 2022; Accepted: 25 July 2022

Published online: 05 August 2022

References

- Wei, T. *et al.* Developed and developing world responsibilities for historical climate change and CO₂ mitigation. *Proc. Natl. Acad. Sci. U.S.A.* **109**, 12911–12915 (2012).
- Davis, S. J., Caldeira, K. & Matthews, H. D. Future CO₂ emissions and climate change from existing energy infrastructure. *Science* **329**, 1330–1333 (2010).
- Matinde, E., Simate, G. S. & Ndlovu, S. Mining and metallurgical wastes: A review of recycling and re-use practices. *J. South Afr. Inst. Min. Metall.* **118**, 825–844 (2018).
- Zhang, L. & Xu, Z. A critical review of material flow, recycling technologies, challenges and future strategy for scattered metals from minerals to wastes. *J. Clean. Prod.* **202**, 1001–1025 (2018).
- Hasan, M. M. *et al.* Intermolecular electron transfer in electrochemically exfoliated BCN-Cu nanosheet electrocatalysts for efficient hydrogen evolution. *ACS Appl. Energy Mater.* <https://doi.org/10.1021/acsaem.2c01349> (2022).
- Gomaa, A. K. *et al.* Facile surface treatment of industrial stainless steel waste meshes at mild conditions to produce efficient oxygen evolution catalysts. *Energy & Fuels* **36**, 7025–7034 (2022).
- Hertwich, E., Lifset, R., Pauliuk, S. & Heeren, N. *Resource Efficiency and Climate Change: Material Efficiency Strategies for a Low-Carbon Future* (United Nations Environment Programme, 2020).
- Salem, K. E. *et al.* Unveiling the optimal interfacial synergy of plasma modulated trimetallic Mn-Ni-Co phosphides: Tailoring deposition ratio for complementary water splitting. *Energy Environ. Mater.* <https://doi.org/10.1002/eem2.12324> (2022).
- Sassenburg, M. Conducting CO₂ reduction at a bipolar membrane electrode assembly (2018).
- Ma, Z. *et al.* Enhanced electrochemical CO₂ reduction of Cu@Cu₂O nanoparticles decorated on 3D vertical graphene with intrinsic sp³-type defect. *Adv. Funct. Mater.* **30**, 1–12 (2020).
- Zhang, R. Z. *et al.* Design strategies and mechanism studies of CO₂ electroreduction catalysts based on coordination chemistry. *Coord. Chem. Rev.* **422**, 1–28 (2020).
- Stolar, T. *et al.* Scalable mechanochemical amorphization of bimetallic Cu-Zn MOF-74 catalyst for selective CO₂ reduction reaction to methanol. *ACS Appl. Mater. Interfaces* **13**, 3070–3077 (2021).
- Li, X. *et al.* Selective electroreduction of CO₂ and CO to C₂H₄ by synergistically tuning nanocavities and the surface charge of copper oxide. *ACS Sustain. Chem. Eng.* <https://doi.org/10.1021/acscuschemeng.2c01600> (2022).
- Hao, L. & Sun, Z. Metal oxide-based materials for electrochemical CO₂ reduction. *Wuli Huaxue Xuebao Acta Phys. Chim. Sin.* **37**, 1–19 (2021).
- Kuhl, K. P., Cave, E. R., Abram, D. N. & Jaramillo, T. F. New insights into the electrochemical reduction of carbon dioxide on metallic copper surfaces. *Energy Environ. Sci.* **5**, 7050–7059 (2012).
- Tomboc, G. M., Choi, S., Kwon, T., Hwang, Y. J. & Lee, K. Potential link between Cu surface and selective CO₂ electroreduction: Perspective on future electrocatalyst designs. *Adv. Mater.* **32**, 1908398 (2020).
- Ghosh, S., Garapati, M. S., Ghosh, A. & Sundara, R. Nonprecious catalyst for three-phase contact in a proton exchange membrane CO₂ conversion full cell for efficient electrochemical reduction of carbon dioxide. *ACS Appl. Mater. Interfaces* **11**, 40432–40442 (2019).
- Li, X., Hong, S., Hao, L. & Sun, Z. Cadmium-based metal-organic frameworks for high-performance electrochemical CO₂ reduction to CO over wide potential range. *Chin. J. Chem. Eng.* **43**, 143–151 (2022).
- Fan, Q. *et al.* Activation of Ni particles into single Ni-N atoms for efficient electrochemical reduction of CO₂. *Adv. Energy Mater.* **10**, 1–8 (2020).
- Bondue, C. J., Graf, M., Goyal, A. & Koper, M. T. M. Suppression of hydrogen evolution in acidic electrolytes by electrochemical CO₂ reduction. *J. Am. Chem. Soc.* **143**, 279–285 (2021).
- Ismail, A. M., Samu, G. F., Balog, Á., Csapó, E. & Janáky, C. Composition-dependent electrocatalytic behavior of Au-Sn bimetallic nanoparticles in carbon dioxide reduction. *ACS Energy Lett.* **4**, 48–53 (2019).
- Mahyoub, S. A. *et al.* Rational design of low loading Pd-alloyed Ag nanocorals for high current density CO₂-to-CO electroreduction at elevated pressure. *Mater. Today Energy* **24**, 100923 (2022).
- Dongare, S., Singh, N. & Bhunia, H. Oxide-derived Cu-Zn nanoparticles supported on N-doped graphene for electrochemical reduction of CO₂ to ethanol. *Appl. Surf. Sci.* **556**, 149790 (2021).
- Dongare, S., Singh, N., Bhunia, H. & Bajpai, P. K. Electrochemical reduction of CO₂ using oxide based Cu and Zn bimetallic catalyst. *Electrochim. Acta* **392**, 138988 (2021).
- Keerthiga, G. & Chetty, R. Electrochemical reduction of carbon dioxide on zinc-modified copper electrodes. *J. Electrochem. Soc.* **164**, H164–H169 (2017).
- Yin, G. *et al.* Selective electro- or photo-reduction of carbon dioxide to formic acid using a Cu-Zn alloy catalyst. *J. Mater. Chem. A* **5**, 12113–12119 (2017).
- Feaster, J. T. *et al.* Understanding selectivity for the electrochemical reduction of carbon dioxide to formic acid and carbon monoxide on metal electrodes. *ACS Catal.* **7**, 4822–4827 (2017).
- He, J., Dettelbach, K. E., Huang, A. & Berlinguette, C. P. Brass and bronze as effective CO₂ reduction electrocatalysts. *Angew. Chem.* **129**, 16806–16809 (2017).
- Jeon, H. S. *et al.* Operando insight into the correlation between the structure and composition of CuZn nanoparticles and their selectivity for the electrochemical CO₂ reduction. *J. Am. Chem. Soc.* **141**, 19879–19887 (2019).
- Lv, J. J. *et al.* A highly porous copper electrocatalyst for carbon dioxide reduction. *Adv. Mater.* **30**, 1–8 (2018).
- Chang, Y. C., Lin, P. S., Liu, F. K., Guo, J. Y. & Chen, C. M. One-step and single source synthesis of Cu-doped ZnO nanowires on flexible brass foil for highly efficient field emission and photocatalytic applications. *J. Alloys Compd.* **688**, 242–251 (2016).
- Zhong, H. *et al.* Synergistic electroreduction of carbon dioxide to carbon monoxide on bimetallic layered conjugated metal-organic frameworks. *Nat. Commun.* **11**, 1–10 (2020).
- Hjorth, I., Nord, M., Rønning, M., Yang, J. & Chen, D. Electrochemical reduction of CO₂ to synthesis gas on CNT supported Cu_xZn_{1-x}O catalysts. *Catal. Today* **357**, 311–321 (2020).
- Miftahurrahman, G., Setiarahayu, H. & Nandiyanto, A. B. D. An economic evaluation on scaling-up production of nano gold from laboratory to industrial scale. *Indones. J. Comput. Eng. Des.* **1**, 29 (2019).
- Tsuzuki, T. Commercial scale production of inorganic nanoparticles. *Int. J. Nanotechnol.* **6**, 567–578 (2009).
- Stojkovic, S. *et al.* Electrocatalyst derived from waste Cu-Sn bronze for CO₂ conversion into CO. *ACS Appl. Mater. Interfaces.* <https://doi.org/10.1021/acsaem.1c05015> (2021).
- Dutta, A., Rahaman, M., Luedi, N. C., Mohos, M. & Broekmann, P. Morphology matters: Tuning the product distribution of CO₂ electroreduction on oxide-derived Cu foam catalysts. *ACS Catal.* **6**, 3804–3814 (2016).
- Li, D. *et al.* Tuning the pore structure of porous tin foam electrodes for enhanced electrochemical reduction of carbon dioxide to formate. *Chem. Eng. J.* **375**, 122024 (2019).
- Hu, H. *et al.* In-situ grown nanoporous Zn-Cu catalysts on brass foils for enhanced electrochemical reduction of carbon dioxide. *Appl. Surf. Sci.* **445**, 281–286 (2018).
- Segall, P. J. D. *et al.* First-principles simulation: Ideas, illustrations and the CASTEP code. *J. Phys. Condens. Matter* **14**, 2717–2744 (2002).

41. Peterson, A. A., Abild-Pedersen, F., Studt, F., Rossmeisl, J. & Nørskov, J. K. How copper catalyzes the electroreduction of carbon dioxide into hydrocarbon fuels. *Energy Environ. Sci.* **3**, 1311–1315 (2010).
42. Ma, M. *et al.* Electrochemical reduction of CO₂ on compositionally variant Au–Pt bimetallic thin films. *Nano Energy* **42**, 51–57 (2017).
43. Dattila, F., Garclá-Muelas, R. & López, N. Active and selective ensembles in oxide-derived copper catalysts for CO₂ reduction. *ACS Energy Lett.* **5**, 3176–3184 (2020).
44. Eissa, D.S., El-Hagar, S.S., Ashour, E.A. & Allam, N.K. Electrochemical nano-patterning of brass for stable and visible light-induced photoelectrochemical water splitting. *Int. J. Hydrogen Energy* **44**, 14588–14595 (2019).
45. Pander, J. E. *et al.* Understanding the heterogeneous electrocatalytic reduction of carbon dioxide on oxide-derived catalysts. *ChemElectroChem* **5**, 219–237 (2018).
46. Varandili, S. B. *et al.* Elucidating the structure-dependent selectivity of CuZn towards methane and ethanol in CO₂ electroreduction using tailored Cu/ZnO precatalysts. *Chem. Sci.* **12**, 14484–14493 (2021).
47. Zoolfakar, A. S., Rani, R. A., Morfa, A. J., O'Mullane, A. P. & Kalantar-Zadeh, K. Nanostructured copper oxide semiconductors: A perspective on materials, synthesis methods and applications. *J. Mater. Chem. C* **2**, 5247–5270 (2014).
48. Li, Y. B., Bando, Y. & Golberg, D. ZnO nanoneedles with tip surface perturbations: Excellent field emitters. *Appl. Phys. Lett.* **84**, 3603–3605 (2004).
49. Li, X. & Wang, Y. Structure and photoluminescence properties of Ag-coated ZnO nano-needles. *J. Alloys Compd.* **509**, 5765–5768 (2011).
50. Allam, N.K., Nazeer, A. A., Youssef, G. I. & Ashour, E. A. Electrochemical and stress corrosion cracking behavior of α -aluminum bronze and α -brass in nitrite solutions: a comparative study. *Corrosion* **69**, 77–84 (2013).
51. Ungár, T. Microstructural parameters from X-ray diffraction peak broadening. *Scr. Mater.* **51**, 777–781 (2004).
52. Bindu, P. & Thomas, S. Estimation of lattice strain in ZnO nanoparticles: X-ray peak profile analysis. *J. Theor. Appl. Phys.* **8**, 123–134 (2014).
53. Kabasakaloğlu, M., Kiyak, T., Şendil, O. & Asan, A. Electrochemical behavior of brass in 0.1 M NaCl. *Appl. Surf. Sci.* **193**, 167–174 (2002).
54. Anantharaj, S., Noda, S., Driess, M. & Menezes, P. W. The pitfalls of using potentiodynamic polarization curves for Tafel analysis in electrocatalytic water splitting. *ACS Energy Lett.* **6**, 1607–1611 (2021).
55. Bayaguud, A., Fu, Y. & Zhu, C. Interfacial parasitic reactions of zinc anodes in zinc ion batteries: Underestimated corrosion and hydrogen evolution reactions and their suppression strategies. *J. Energy Chem.* **64**, 246–262 (2022).
56. Nguyen, D. L. T. *et al.* Effect of halides on nanoporous Zn-based catalysts for highly efficient electroreduction of CO₂ to CO. *Catal. Commun.* **114**, 109–113 (2018).
57. Botz, A. J. R., Nebel, M., Rincón, R. A., Ventosa, E. & Schuhmann, W. Onset potential determination at gas-evolving catalysts by means of constant-distance mode positioning of nanoelectrodes. *Electrochim. Acta* **179**, 38–44 (2015).
58. Jiang, K. *et al.* Effects of surface roughness on the electrochemical reduction of CO₂ over Cu. *ACS Energy Lett.* **5**, 1206–1214 (2020).
59. Tang, W. *et al.* The importance of surface morphology in controlling the selectivity of polycrystalline copper for CO₂ electroreduction. *Phys. Chem. Chem. Phys.* **14**, 76–81 (2012).
60. Ajmal, S. *et al.* Zinc-modified copper catalyst for efficient (photo-)electrochemical CO₂ reduction with high selectivity of HCOOH production. *J. Phys. Chem. C* **123**, 11555–11563 (2019).
61. Feng, Y. *et al.* Laser-prepared CuZn alloy catalyst for selective electrochemical reduction of CO₂ to ethylene. *Langmuir* **34**, 13544–13549 (2018).
62. Goyal, A., Marcandalli, G., Mints, V. A. & Koper, M. T. M. Competition between CO₂ reduction and hydrogen evolution on a gold electrode under well-defined mass transport conditions. *J. Am. Chem. Soc.* **142**, 4154–4161 (2020).
63. Dunwell, M. *et al.* Examination of near-electrode concentration gradients and kinetic impacts on the electrochemical reduction of CO₂ using surface-enhanced infrared spectroscopy. *ACS Catal.* **8**, 3999–4008 (2018).
64. Zeng, J. *et al.* Coupled copper–zinc catalysts for electrochemical reduction of carbon dioxide. *ChemSuschem* **13**, 4128–4139 (2020).
65. Mohamed, A. G. A. *et al.* Asymmetric oxo-bridged ZnPb bimetallic electrocatalysis boosting CO₂-to-HCOOH reduction. *Adv. Sci.* **2104138**, 1–10 (2021).
66. Chen, T. L. *et al.* In situ unraveling of the effect of the dynamic chemical state on selective CO₂ reduction upon zinc electrocatalysts. *Nanoscale* **12**, 18013–18021 (2020).
67. Daiyan, R. *et al.* Uncovering atomic-scale stability and reactivity in engineered zinc oxide electrocatalysts for controllable syngas production. *Adv. Energy Mater.* **10**, 1–9 (2020).
68. Lu, Q. *et al.* Uniform Zn deposition achieved by Ag coating for improved aqueous zinc-ion batteries. *ACS Appl. Mater. Interfaces* **13**, 16869–16875 (2021).
69. Nunomura, N. Density functional theory study of Cu–Zn alloys. **902012035**, 7–10 (2012).
70. Nitopi, S. *et al.* Progress and perspectives of electrochemical CO₂ reduction on copper in aqueous electrolyte. *Chem. Rev.* <https://doi.org/10.1021/acs.chemrev.8b00705> (2019).
71. Liu, L. & Lv, P. DFT insight into the effect of Cu atoms on adsorption and dissociation of CO₂ over a Pd₈/TiO₂(101) surface. *RSC Adv.* **11**, 17391–17398 (2021).
72. Jiao, S., Fu, X. & Huang, H. Descriptors for the evaluation of electrocatalytic reactions: d-band theory and beyond. *Adv. Funct. Mater.* **32**, 1–43 (2022).
73. Zhang, Z. *et al.* ‘Two ships in a bottle’ design for Zn–Ag–O catalyst enabling selective and long-lasting CO₂ electroreduction. *J. Am. Chem. Soc.* **143**, 6855–6864 (2021).
74. Xiao, J. & Frauenheim, T. Theoretical insights into CO₂ activation and reduction on the Ag(111) monolayer supported on a ZnO(0001) substrate. *J. Phys. Chem. C* **117**, 1804–1808 (2013).
75. Nørskov, J. K., Bligaard, T., Rossmeisl, J. & Christensen, C. H. Towards the computational design of solid catalysts. *Nat. Chem.* **1**, 37–46 (2009).
76. Xiao, J. & Frauenheim, T. Theoretical insights into CO₂ activation and reduction on the Ag(111) monolayer supported on a ZnO(0001) substrate. *J. Phys. Chem. C* **117**, 1804–1808 (2013).

Author contributions

I.M.B. carried out the experimental work and wrote the manuscript with support from A.M.I. G.E.K. carried out the DFT calculations and wrote the corresponding section, while M.M.T. was responsible for the HPLC measurements. N.K.A. analyzed the results, wrote the manuscript, secured the funding, and supervised the work. All authors have given approval to the final version of the manuscript.

Funding

Open access funding provided by The Science, Technology & Innovation Funding Authority (STDF) in cooperation with The Egyptian Knowledge Bank (EKB). This study was funded by the Climate Change Funding from AUC (No. CCI-SSE-PHYS-08).

Competing interests

The authors declare no competing interests.

Additional information

Supplementary Information The online version contains supplementary material available at <https://doi.org/10.1038/s41598-022-17317-6>.

Correspondence and requests for materials should be addressed to N.K.A.

Reprints and permissions information is available at www.nature.com/reprints.

Publisher's note Springer Nature remains neutral with regard to jurisdictional claims in published maps and institutional affiliations.



Open Access This article is licensed under a Creative Commons Attribution 4.0 International License, which permits use, sharing, adaptation, distribution and reproduction in any medium or format, as long as you give appropriate credit to the original author(s) and the source, provide a link to the Creative Commons licence, and indicate if changes were made. The images or other third party material in this article are included in the article's Creative Commons licence, unless indicated otherwise in a credit line to the material. If material is not included in the article's Creative Commons licence and your intended use is not permitted by statutory regulation or exceeds the permitted use, you will need to obtain permission directly from the copyright holder. To view a copy of this licence, visit <http://creativecommons.org/licenses/by/4.0/>.

© The Author(s) 2022